Supplemental Information

Demystifying Metal-Assisted Chemical Etching of GaN and Related Multi-Heterojunctions

Clarence Y. Chan,[1] Jan Paul Menzel,[2] Yicong Dong,[1] Zhuoran Long,[2] Aadil Waseem,[3] Xihang Wu,[3] Yixin Xiao,[4] Andy Xie,[5] Edmond K. C. Chow,[1] Victor S. Batista,[2] Shaloo Rakheja,[1] Zetian Mi,[4] and Xiuling Li[1,3*]

[1]*Department of Electrical and Computer Engineering, Holonyak Micro and Nanotechnology Laboratory, University of Illinois at Urbana-Champaign, Urbana, IL, 61801, USA*
[2]*Department of Chemistry and Energy Sciences Institute, Yale University, West Haven, CT, 06516, USA*
[3]*Department of Electrical and Computer Engineering, Microelectronics Research Center, The University of Texas, Austin, TX, 78758, USA*
[4]*Department of Electrical Engineering and Computer Science, University of Michigan, Ann Arbor, MI, 48109 USA*
[5]*Qorvo, Richardson, TX, 75080, USA*

*Corresponding author e-mail address: xiuling.li@utexas.edu

Figure S1: 3 mm x 3 mm pattern field with randomly scaled features

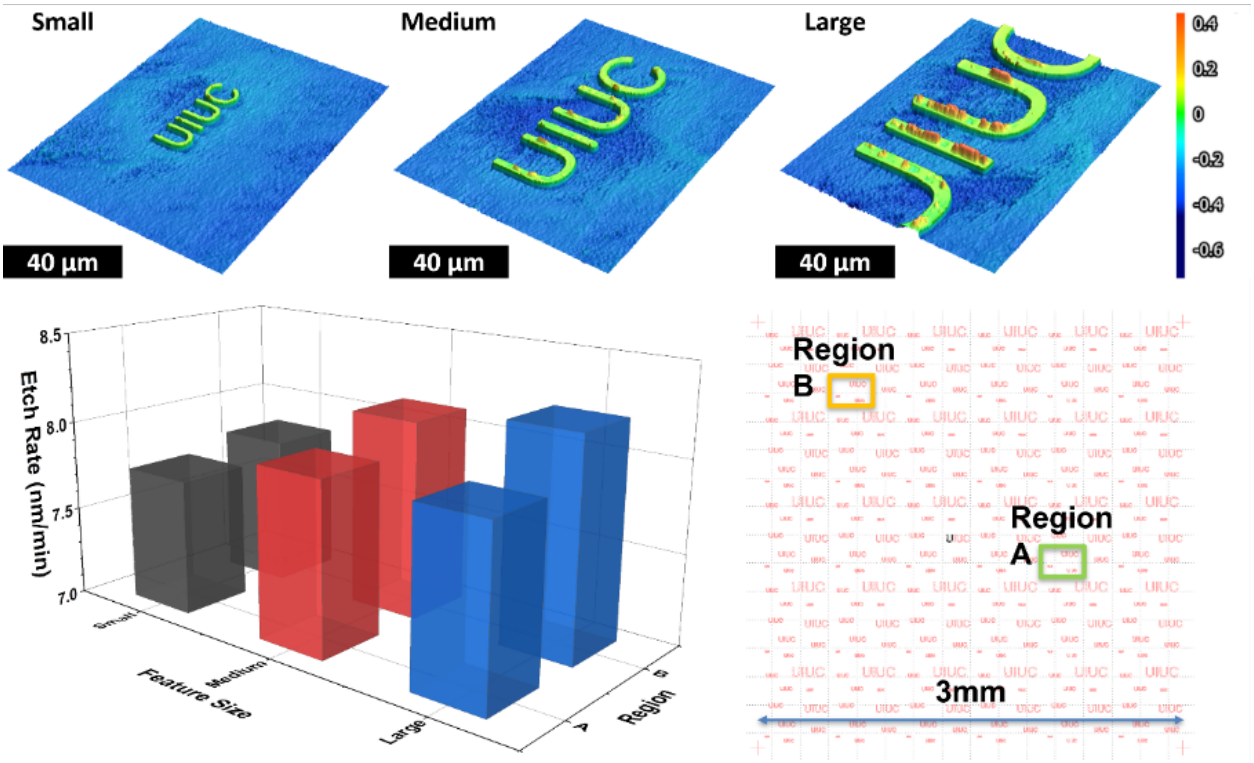

Optical profile scans (top row) and measured etch rate plot (bottom left) of randomly selected regions A and B, as indicated, in a 3mm x 3mm pattern field (bottom right). Color scale (upper right) for the optical profile scans is in µm. Etch rate variation of the UIUC lettering in different regions across a distance of ~ 2.5 mm is found to be only ~ 6% from 7.7 to 8.2 nm/min, with the smaller features showing slower etch rate.

Figure S2: Effect if solution concentration on etch rate

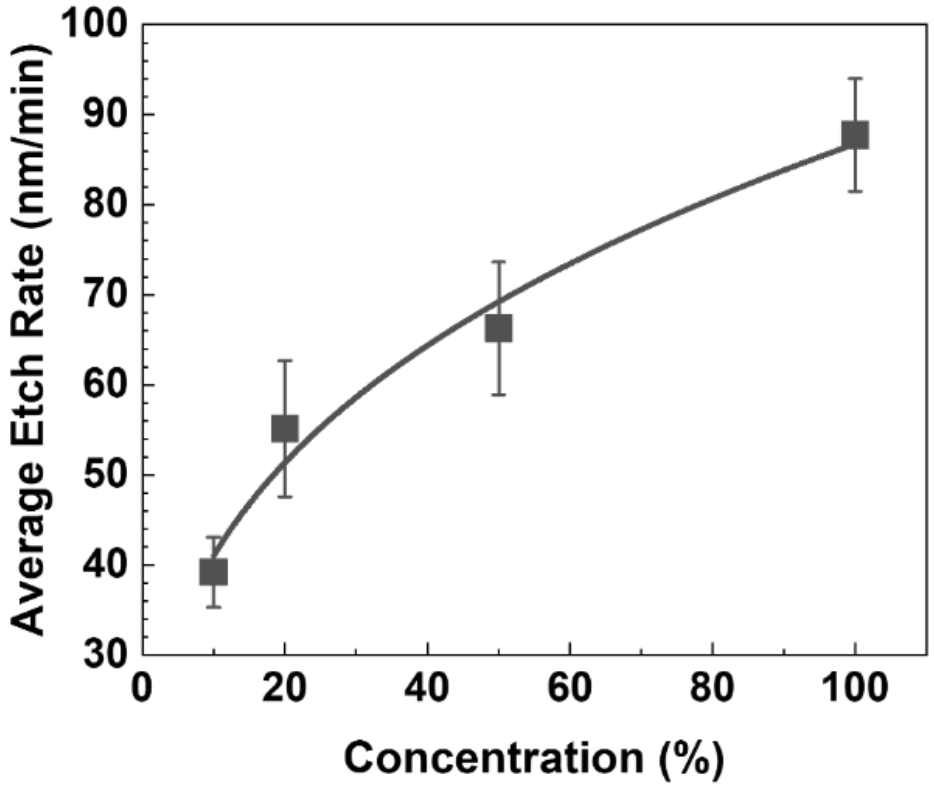

Effect of solution concentration (HCl etchant with $K_2S_2O_8$ oxidant at a 1:12 molar ratio) on n-GaN MacEtch rate. It is observed that with 10x dilution of the MacEtch solution, the average etch rate is sub-linear and is only reduced by about 50% which would not be expected in a purely chemical-based etchant.

Figure S3: Metal catalyst undercut vs. solution concentration and oxidant ratio

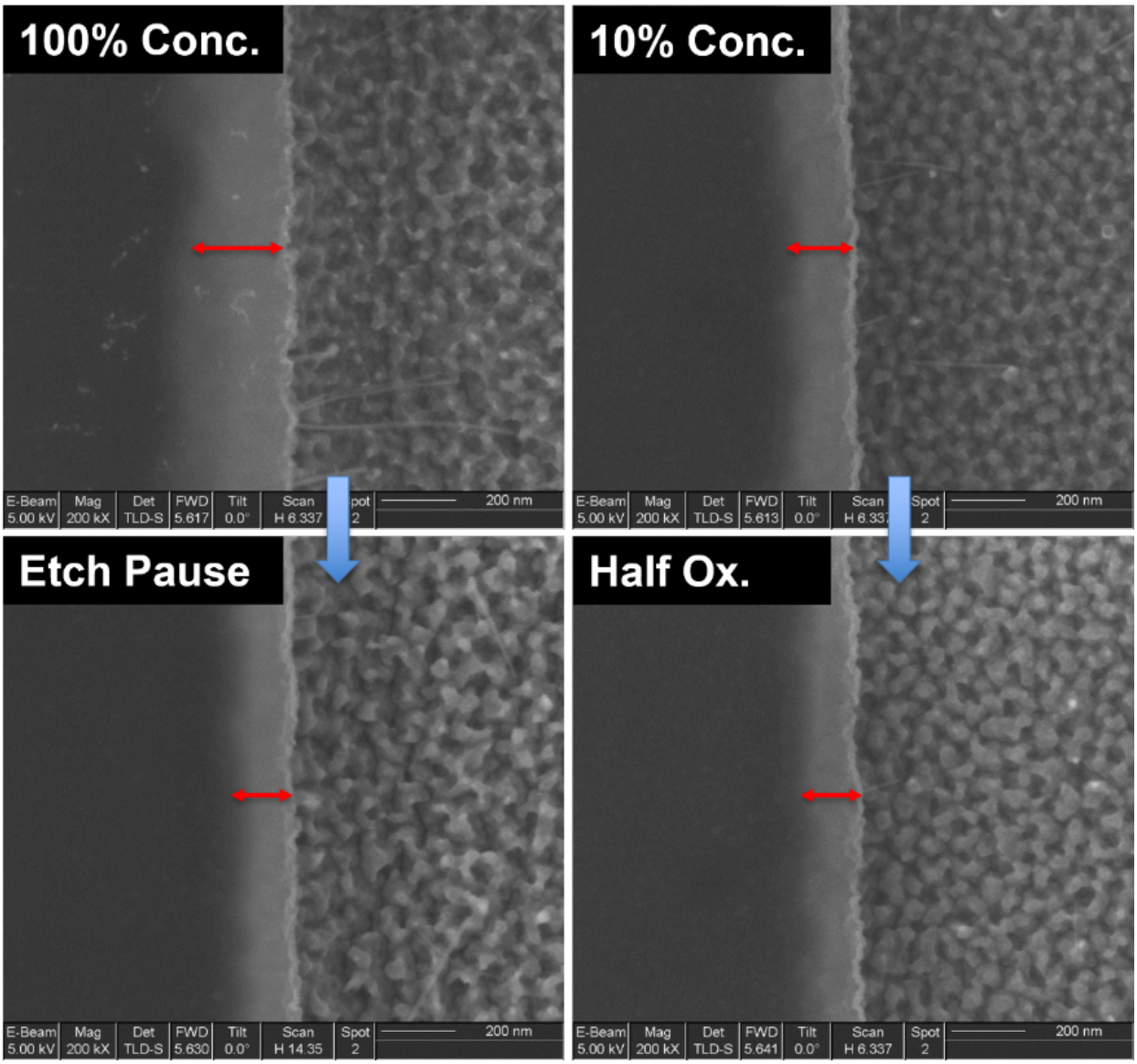

SEM micrographs depicting undercut of the metal catalyst (marked by red arrows) with the 100% concentration as the control. When the solution is diluted by 10x (10% conc.), it is found that the undercut is reduced. It is also found that for a 10% conc. solution with half the oxidant concentration, the undercut is not significantly altered suggesting that the oxidant is not the primary source of the phenomena. At the same time, with a 100% conc. solution, we find that if the etch is paused mid-way and re-started such that the total etch time is the same, the undercut is reduced suggesting the source is a temporally evolved agent produced in the solution over time.

Figure S4: Etch uniformity of heated and unheated solutions based on KOH

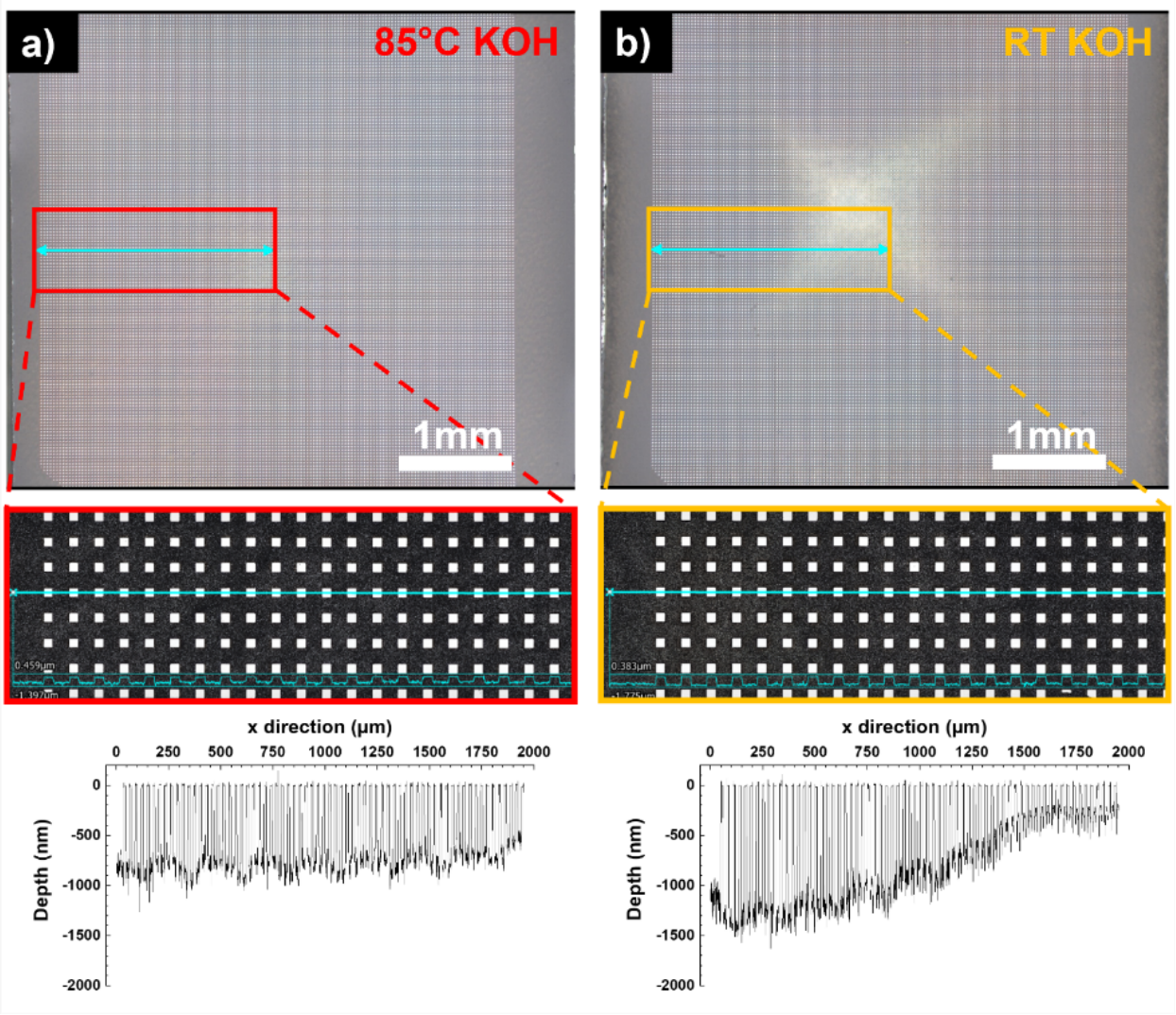

Etch uniformity across a mm scale is found to only be present for KOH etch solutions when heated. The unheated solution shows a distinct parabolic etch profile whereby the etch depth is shallower towards the middle of the pattern field as compared to the edges. Conversely, the profile for room temperature HCl etches is identical to that of heated KOH suggesting better mass transport in the former. The etch depth for heated KOH is around 900 nm while the unheated KOH varies from almost 1500 nm to 500 nm (pattern edge to center).

TCAD Simulation Methodology

In the TCAD simulation framework, we solve for 3-D drift-diffusion transport at steady-state using the Finite Element Method (FEM) with Newton iterations in Sentaurus. The grid is set to be denser at the top of the wafer where where crucial transport effects must be captured and coarser near the bottom of the substrate. Equations solved for drift-diffusion transport are the Shockley equations, amongst which is Gauss' Law that governs the coupling between electrostatic potential and space charge:

$$\nabla \cdot (\epsilon_r \epsilon_0 \nabla \phi) = -q(p - n + N_{\text{sd}}^{+} - N_{\text{da}}^{-}),$$

where $\epsilon_r = 8.9$ is relative permittivity of GaN, ϵ_0 is vacuum permittivity, ϕ is the electrostatic potential, q is elementary charge, p is the free hole density, n is the free electron density, N_{sd}^{+} is the ionized shallow donor density, and N_{da}^{-} is the ionized deep acceptor density.

In the case of our samples, we adopt $N_{\text{sd}} = 5 \times 10^{18}$ cm^{-3} as the intentional silicon shallow donor concentration and $N_{\text{da}} = 10^{17}$ cm^{-3} as the unintentional carbon deep-level acceptor defect concentration so that the sample resistivity agrees with experiment around 0.02 Ω.cm. With Fermi-Dirac statistics, one can expand each term of the right hand side of Gauss' Law as:

$$p = N_V \mathcal{F}_{1/2}\left(\frac{E_V - F_p}{k_B T}\right),$$
$$n = N_C \mathcal{F}_{1/2}\left(\frac{F_n - E_C}{k_B T}\right),$$
$$N_{\text{sd}}^{+} = \frac{N_{\text{sd}}}{1 + 2\frac{\mathcal{F}_{1/2}\left(\frac{F_n - E_C}{k_B T}\right)}{\mathcal{F}_{1/2}\left(\frac{E_{\text{sd}} - E_C}{k_B T}\right)}},$$
$$N_{\text{da}}^{-} = \frac{N_{\text{da}}}{1 + \frac{\mathcal{F}_{1/2}\left(\frac{E_V - F_p}{k_B T}\right)}{\mathcal{F}_{1/2}\left(\frac{E_V - E_{\text{da}}}{k_B T}\right)}},$$

where $N_V = 4.6 \times 10^{19}$ cm^{-3} is the valance band effective density of states, $N_C = 2.3 \times 10^{18}$ cm^{-3} is the conduction band effective density of states, $\mathcal{F}_{1/2}$ is Fermi integral of order 1/2, E_V is the valence band maximum, E_C is the conduction band minimum, F_p is hole quasi-Fermi level, F_n is electron quasi-Fermi level, $E_{\text{sd}} = E_C - 0.0225$ eV is the shallow donor silicon energy [Y1], $E_{\text{da}} = E_V + 0.9$ eV is the deep acceptor carbon energy [Y2], $k_B = 8.617 \times 10^{-5}$ eV/K is the Boltzmann constant, and $T = 300$ K is the simulation temperature. Note that for wurtzite GaN, bandgap $E_G = E_C - E_V = 3.457$ eV.

The remainder of the Shockley equations we solve are the continuity equations:

$$\mathrm{q}\frac{\partial n}{\partial \mathrm{t}} = 0 = \nabla \cdot \overrightarrow{J_n} - \mathrm{q}\left(R_{\text{SRH}}^{n} + R_{\text{rad}}^{n} - G_{\text{opt},n}\right),$$
$$\mathrm{q}\frac{\partial p}{\partial \mathrm{t}} = 0 = -\nabla \cdot \overrightarrow{J_p} - \mathrm{q}\left(R_{\text{SRH}}^{p} + R_{\text{rad}}^{p} - G_{\text{opt},p}\right),$$

where $\overrightarrow{J_n}\left(\overrightarrow{J_p}\right)$ is the electron (hole) current density, $R_{\text{SRH}}^{n}\left(R_{\text{SRH}}^{p}\right)$ is the electron (hole) Shockley-Read-Hall recombination rate with recombination time constant nominally set to 1 ns [Y3, Y4] for

both carriers, $R_{\text{rad}}^{n}\left(R_{\text{rad}}^{p}\right)$ is the electron (hole) radiative recombination rate, G_{opt} is the optical generation rate, and we set time derivatives of the electron (hole) concentration to zero for steady-state simulations. We also set radiative recombination rates to zero because the simulation is under low-level injection condition for the given optical intensity. In addition, electron and hole currents are given as:

$$\overrightarrow{J_n} = \mathrm{q}D_n\nabla n + \mathrm{qn}\mu_n\vec{\mathcal{E}},$$
$$\overrightarrow{J_p} = -\mathrm{q}D_p\nabla p + \mathrm{qp}\mu_p\vec{\mathcal{E}},$$

where $D_n\left(D_p\right)$ is the electron (hole) diffusion coefficient, $\mu_n = 250\ \text{cm}^2/\text{V.s}$ $\left(\mu_{\text{p}} = 12.5\ \text{cm}^2/\text{V.s}\right)$ is the constant electron (hole) drift mobility set for the given total doping concentration [Y5, Y6], and $\vec{\mathcal{E}}$ is the electric field.

For optical injection, we use Beer's Law to calculate generation rate with monochromatic light at normal incidence to the top of the wafer with 100% quantum efficiency. Optical generation rate is thus given as:

$$G_{\text{opt}}(x,t) = \frac{I(y,z)\lambda}{hc}\alpha e^{-\alpha \mathrm{x}}$$

where x is direction normal to the wafer substrate, y and z are parallel to the wafer surface, $\frac{\lambda}{hc}$ is the inverse of single photon energy of 3.457 eV which equates the bandgap energy, $\alpha = 9.00\ \mu\text{m}^{-1}$ is the absorption coefficient for light wavelength compatible with the 3.457 eV single photon energy [Y7], and $I(y,z)$ is the incident areal optical power density.

To study the impact of feature sizes, we perform four sets of simulations where we fix the feature spacings $L_s = 4.8\ \mu\text{m}$ and vary the feature sizes $L_d = \{2.4, 4.8, 7.2, 9.6\}\ \mu\text{m}$. Both the total wafer area and the total feature area are conserved, so the mesa outer rim to wafer boundaries distance is the smallest at 35 μm for $L_d = 2.4\ \mu\text{m}$ and largest at 78.2 μm for $L_d = 9.6\ \mu\text{m}$. To study the impact of radial distributions, we conduct four additional sets of simulations with conserved total wafer area and fixed 16 total features. We fix $L_d = 9.6\ \mu\text{m}$ and vary $L_s = \{4.8, 12, 29.723, 109.4769\}\ \mu\text{m}$. The mesa outer rim to wafer boundaries distance is smallest at 25 μm for $L_s = 109.4769\ \mu\text{m}$ and largest at 182.0 μm for $L_s = 4.8\ \mu\text{m}$. At regions where the features reside $I(y,z) = 0$, and at spacings between the features, we set $I(y,z) = 5.5\ \text{W/cm}^2$ which is the mercury lamp intensity. Spacings are grounded with $V_s = 0\ \text{V}$, and features are biased at $V_d = 3.95\ \text{V}$. This is estimated based on approximating the charge extraction with the diode equation.

For each of the simulations, we take a cut plane 1 nm beneath the wafer surface, and on the cut plane, we use a cut line through the center of one row of mesa features. At this cut line, we obtain the spatial distribution of hole concentration. Because the spacings between features have much higher hole density when the mesas have extracted most of the electrons, these spacings are regions that MacEtch takes place. As a result, the average hole concentration is extracted at the spacings for each simulation, which we then compare with the etch rate at the spacings on dual y-axis Fig. 3e) and f).

Section References:

[Y1] J. T. Torvik, 'Dopants in GaN', in *III-Nitride Semiconductors: Electrical, Structural and Defects Properties*, Elsevier, 2000, pp. 17–49.

[Y2] A. Chini *et al.*, 'Experimental and numerical analysis of hole emission process from carbon-related traps in GaN buffer layers', *IEEE Transactions on Electron Devices*, vol. 63, no. 9, pp. 3473–3478, 2016.

[Y3] S. J. Pearton, C. R. Abernathy, and F. Ren, 'Design and fabrication of gallium high-power rectifiers', *Gallium Nitride Processing for Electronics, Sensors and Spintronics*, pp. 179–212, 2006.

[Y4] S. Rakheja, K. Li, K. M. Dowling, A. M. Conway, and L. F. Voss, 'Design and simulation of near-terahertz GaN photoconductive switches--operation in the negative differential mobility regime and pulse compression', *IEEE Journal of the Electron Devices Society*, vol. 9, pp. 521–532, 2021.

[Y5] V. W. L. Chin, T. L. Tansley, and T. Osotchan, 'Electron mobilities in gallium, indium, and aluminum nitrides', *Journal of Applied Physics*, vol. 75, no. 11, pp. 7365–7372, 1994.

[Y6] D. K. Gaskill, L. B. Rowland, and K. Doverspike, 'Electrical transport properties of AlN, GaN and AlGaN', *Properties of group III nitrides*, vol. 11, pp. 101–116, 1995.

[Y7] J. F. Muth *et al.*, 'Absorption coefficient and refractive index of GaN, AlN and AlGaN alloys', *Materials Research Society Internet Journal of Nitride Semiconductor Research*, vol. 4, no. S1, pp. 502–507, 1999.

DFT Simulation Methodology

DFT calculations to determine the spatial distribution of the band edge states were performed using the Vienna Ab initio Simulation Package (VASP5.4.1)[1–3] using the PBE exchange correlation functional[4,5]. The core electrons, including the 3d electrons for Gallium, were described using Projected-Augmented Wave potentials (PAWs),[6,7] with dispersion interactions included via the BJ-damping corrected DFT-D3 method.[8,9] energy cutoff for the plane waves was set to 500 eV, with convergence for energy and forces set to 10^{-6} eV and 0.02 eV/Å respectively. A Gaussian smearing function with a σ value of 0.1 eV was used. The GaN supercell was constructed from optimized bulk geometry, rotated with the GaN($10\bar{1}0$) plane normal parallel to the *z*-direction. The simulation box with periodic boundary conditions and the dimensions of 6.389 Å x 10.421 Å x 30.000 Å contains a total of 14 layers, with 4 Ga and 4 N atoms in each layer, respectively. As water tends to dissociate on the GaN($10\bar{1}0$) surface,[10] hydroxides were placed on the Gallium sites of the surface layers, with protons covering the nitrogen sites. In total, this results in a simulation box containing a total of 136 atoms, with a vacuum layer of approximately 8 Å to prevent interactions of the slab with itself over the box border in z-direction. A Monkhorst-type k-grid with 3x3x1 k-points was employed. The projected density of states (PDOS) data are prepared using the VASPKIT package.[11] To visualize both geometries and spatial distribution of the band states, the VESTA program was used.[12] The structure, with the dissociated water and the upper and lower two layers was allowed to relax to the new environment, while the central 10 layers were frozen in bulk geometry to maintain bulk properties. A representation of the simulation box is given in figure S5.

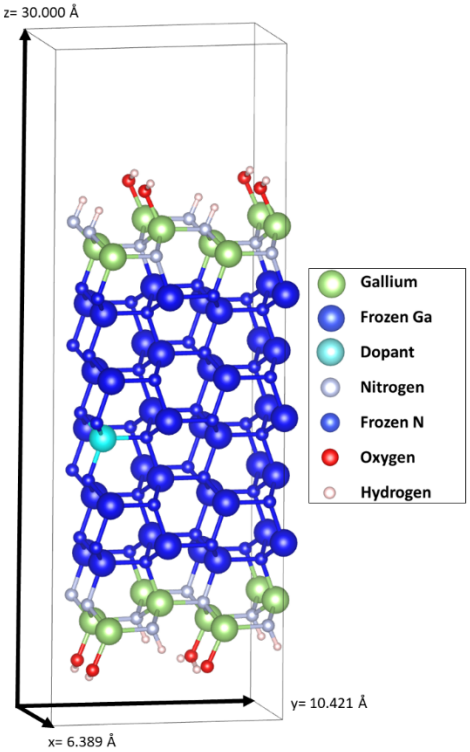

Figure S5: Simulation box used in the DFT analysis. Given in dark blue are the atoms frozen in bulk geometry, while the cyan atom denotes the site which is exchanged either by Ga (intrinsic GaN), Mg (p-doped) or Si (n-doped)

Doping was represented with the exchange of a single Ga atom by a Mg or Si atom for p-type and n-type doping respectively. It is important to note, that this results in a much higher dopant concentration than is physical, but appropriate to obtain qualitative trends. Due to the implementation into a foreign crystal, the Si and Mg atoms will be forced into close to the same crystal structure as the native GaN, allowing for distortion would have too large effects in our model due to the high dopant level and relatively small simulation box. Therefore, the dopant atoms are also frozen in their positions in the bulk layers. The effect on the valence band maximum was investigated, neglecting the singly occupied state introduced by the dopant atom, since these states will be neglectable in a system with physical dopant levels, which are extremely low. These singly occupied states are given in figure S6.

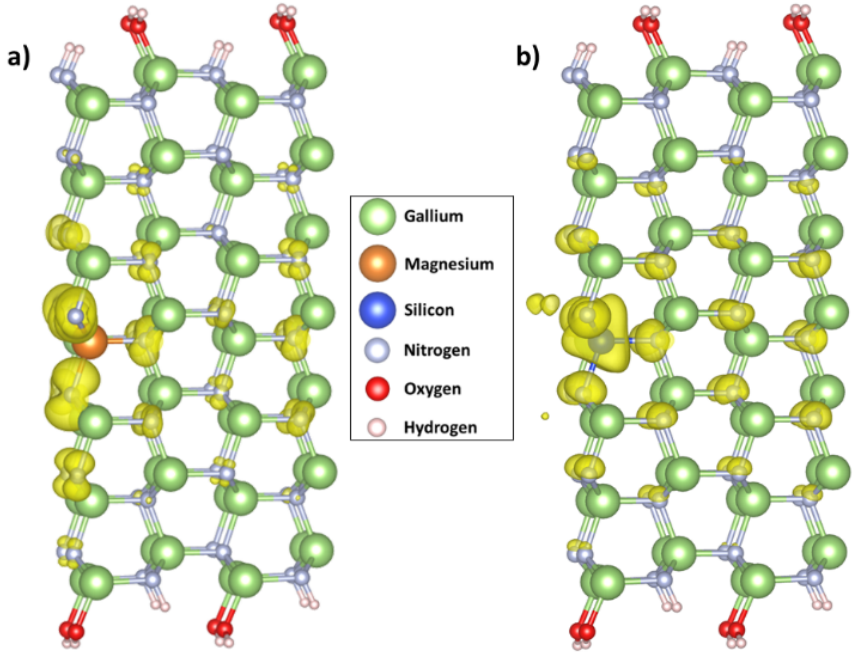

Figure S6: Singly occupied states of the p-doped (a) and n-doped (b) GaN.

The conduction band maxima and valence band minima of each case, doped and intrinsic, are given in figure S7.

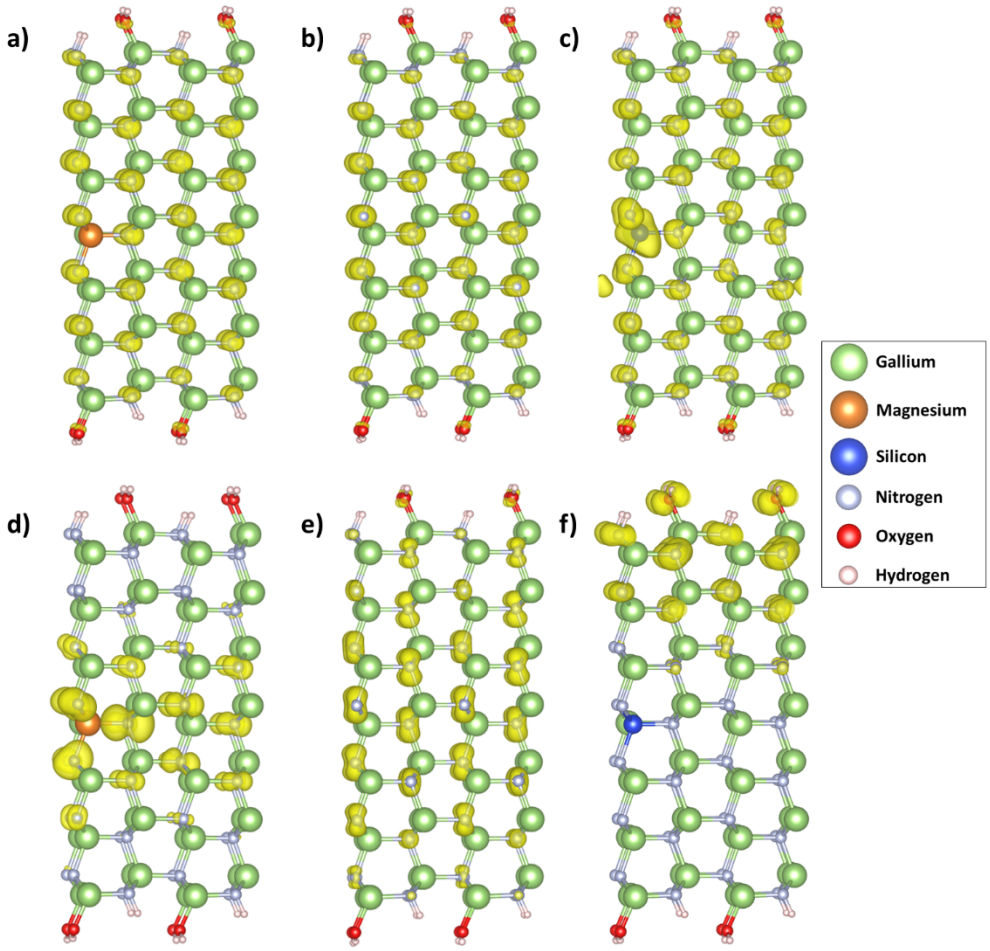

Figure S7: Spatial distribution of the band states representing the Conduction band minimum (top) of p-doped GaN (a), intrinsic GaN (b) and n-doped GaN (c), as well as the valence band maxima in p-doped GaN (d), intrinsic GaN (e) and n-doped GaN (f).

Additionally, we performed a Density of States analysis on the three different systems, dissecting the surface (unfrozen) and bulk (frozen) parts of the simulation box. These are given in figure S8 for p-doped, intrinsic and n-doped GaN.

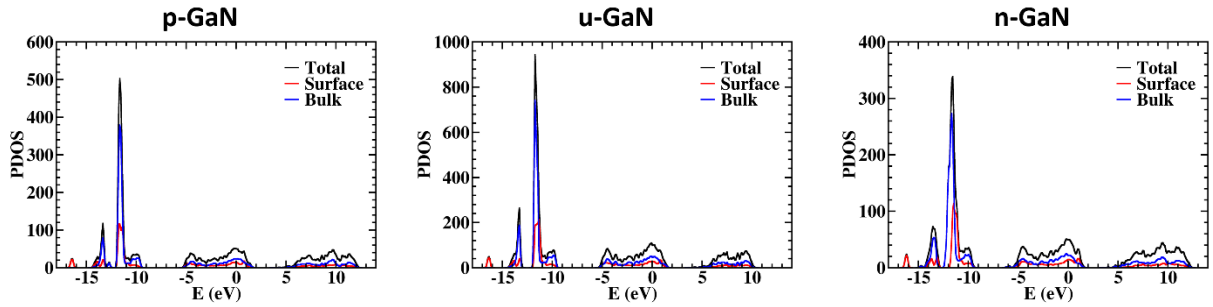

Figure S8 Density of states (DOS) and projected density of states (PDOS) on surface and bulk-like atoms for p-GaN (Mg-doped), u-GaN and n-GaN (Si-doped). Zoom-in plots around the GaN band gap are shown in Figure 5 of the main content. The surface atoms are Ga and N atoms in the upper / lower two layers and O and H atoms from the dissociated water, which are relaxed during the geometry optimization. The rest atoms are bulk-like since they are frozen during the geometry optimization.

Section References:

(1) Kresse, G.; Hafner, J. Ab Initio Molecular Dynamics for Liquid Metals. *Phys. Rev. B* **1993**, *47* (1), 558–561. https://doi.org/10.1103/PhysRevB.47.558.

(2) Kresse, G.; Furthmüller, J. Efficient Iterative Schemes for Ab Initio Total-Energy Calculations Using a Plane-Wave Basis Set. *Phys. Rev. B* **1996**, *54* (16), 11169–11186. https://doi.org/10.1103/PhysRevB.54.11169.

(3) Kresse, G.; Furthmüller, J. Efficiency of Ab-Initio Total Energy Calculations for Metals and Semiconductors Using a Plane-Wave Basis Set. *Comput. Mater. Sci.* **1996**, *6* (1), 15–50. https://doi.org/10.1016/0927-0256(96)00008-0.

(4) Perdew, J. P.; Burke, K.; Ernzerhof, M. Generalized Gradient Approximation Made Simple. *Phys Rev Lett* **1996**, *77* (18), 3865–3868.

(5) Perdew, J. P.; Burke, K.; Ernzerhof, M. Generalized Gradient Approximation Made Simple [Phys. Rev. Lett. 77, 3865 (1996)]. *Phys Rev Lett* **1997**, *78* (7), 1396–1396.

(6) Kresse, G.; Hafner, J. Norm-Conserving and Ultrasoft Pseudopotentials for First-Row and Transition Elements. *J. Phys. Condens. Matter* **1994**, *6* (40), 8245. https://doi.org/10.1088/0953-8984/6/40/015.

(7) Kresse, G.; Joubert, D. From Ultrasoft Pseudopotentials to the Projector Augmented-Wave Method. *Phys. Rev. B* **1999**, *59* (3), 1758–1775. https://doi.org/10.1103/PhysRevB.59.1758.

(8) Grimme, S.; Antony, J.; Ehrlich, S.; Krieg, H. A Consistent and Accurate Ab Initio Parametrization of Density Functional Dispersion Correction (DFT-D) for the 94 Elements H-Pu. *J. Chem. Phys.* **2010**, *132* (15), 154104. https://doi.org/10.1063/1.3382344.

(9) Grimme, S.; Ehrlich, S.; Goerigk, L. Effect of the Damping Function in Dispersion Corrected Density Functional Theory. *J. Comput. Chem.* **2011**, *32* (7), 1456–1465. https://doi.org/10.1002/jcc.21759.

(10) Wang, J.; Pedroza, L. S.; Poissier, A.; Fernández-Serra, M. V. Water Dissociation at the GaN(10$\bar{1}$0) Surface: Structure, Dynamics and Surface Acidity. *J. Phys. Chem. C* **2012**, *116* (27), 14382–14389. https://doi.org/10.1021/jp302793s.

(11) V. Wang, N. Xu, J.C. Liu, G. Tang, W.T. Geng, VASPKIT: A User-Friendly Interface Facilitating High-Throughput Computing and Analysis Using VASP Code, Computer Physics Communications 267, 108033 (2021). https://doi.org/10.1016/j.cpc.2021.108033.
(12) Momma, K.; Izumi, F. VESTA 3 for Three-Dimensional Visualization of Crystal, Volumetric and Morphology Data. *J. Appl. Crystallogr.* **2011**, *44* (6), 1272–1276. https://doi.org/10.1107/S0021889811038970.